

Gravitational wave signatures from the phase-transition-induced collapse of a magnetized neutron star

Anson Ka Long Yip^{1,*}, Patrick Chi-Kit Cheong^{2,3}, and Tjonnie Guang Feng Li^{1,4,5}

¹Department of Physics, The Chinese University of Hong Kong, Shatin, N. T., Hong Kong

²Department of Physics and Astronomy, University of New Hampshire, 9 Library Way, Durham NH 03824, USA

³Department of Physics, University of California, Berkeley, Berkeley, CA 94720, USA

⁴Institute for Theoretical Physics, KU Leuven, Celestijnenlaan 200D, B-3001 Leuven, Belgium

⁵Department of Electrical Engineering (ESAT), KU Leuven, Kasteelpark Arenberg 10, B-3001 Leuven, Belgium

*klyip@phy.cuhk.edu.hk

ABSTRACT

Strong magnetic fields make neutron stars potential sources of detectable electromagnetic and gravitational-wave signals. Hence, inferring these magnetic fields is critical to understand the emissions of neutron stars. However, due to the lack of direct observational evidence, the interior magnetic field configuration remains ambiguous. Here, for the first time, we show that the internal magnetic field strength along with the composition of a neutron star can be directly constrained by detecting the gravitational waves from the *phase-transition-induced collapse* of a magnetized neutron star. By dynamically simulating this collapsing event, we first find that the dominant peaks in the gravitational waveform are the fundamental $l = 0$ quasi-radial F mode and the fundamental $l = 2$ quadrupolar 2f mode. We next show that the maximum gravitational wave amplitude $|h|_{\max}$ increases with the maximum magnetic field strength of the interior toroidal field \mathcal{B}_{\max} until the maximum rest-mass density at bounce $\rho_{\max,b}$ decreases due to the increasing \mathcal{B}_{\max} . We then demonstrated that the magnetic suppression of fundamental modes found in our previous work remains valid for the hybrid stars formed after the phase-transition-induced collapses. We finally show that measuring the frequency ratio between the two fundamental modes f_{2f}/f_F allows one to infer \mathcal{B}_{\max} and the baryonic mass fraction of matter in the mixed phase M_{mp}/M_0 of the resulting hybrid star. Consequently, taking \mathcal{B}_{\max} and M_{mp}/M_0 as examples, this work has demonstrated that much information inside neutron stars could be extracted similarly through measuring the oscillation modes of the stars.

Introduction

The strongest magnetic fields in the universe, up to 10^{14-15} G, are discovered on the surface of neutron stars. Some puzzling astronomical phenomena can be explained by these highly magnetized neutron stars, including soft gamma-ray repeaters and anomalous X-ray pulsars¹⁻⁵. Besides, it has been demonstrated that ultrahigh magnetic fields can deform neutron stars based on the field geometry. Neutron stars become prolate by a purely toroidal field⁶⁻⁸, while they become oblate by a purely poloidal field⁹⁻¹¹. These deformations make rotating neutron stars possible sources of continuous gravitational waves¹².

As the magnetic field governs the emissions of neutron stars, it is vital to interpret the magnetic field configurations of neutron stars. With radio astronomical data, the dipole-spin-down model is typically used to estimate the surface magnetic field strength of neutron stars^{13,14}. Recently, the Neutron Star Interior Composition Explorer (NICER) also allows for the deduction of the geometry and strength of the surface magnetic field from the X-ray emitting hotspots in pulsars^{15,16}. Nevertheless, all these measurements can only provide clues to the surface magnetic field but not the interior magnetic field of neutron stars. Therefore, it is still challenging to determine the nature of the magnetic field inside neutron stars.

Detection of gravitational-wave signals from neutron stars provides a novel way of probing information inside the stars. The first signal detected was produced by a binary neutron star merger GW170817¹⁷. Aside from merger events, the phase-transition-induced collapse of a neutron star is also a potential scenario for producing observable gravitational wave signals. When the rest-mass density in the neutron star core exceeds a certain threshold, a gravitational collapse is triggered by the phase transition from hadronic matter to deconfined quark matter in the core. This collapse results in a more compact ‘hybrid star’ composed of hadrons and deconfined quarks. This collapse could occur in a newly born neutron star from a supernova explosion and an accreting neutron star in a binary system^{18,19}. Dynamical simulations were employed to study the dynamics and gravitational-wave signals of such a phase-transition-induced collapse^{19,20}. In particular, they initiated the phase-transition-induced collapse by replacing the original polytropic equation of state with a ‘softer’ equation of state that

takes deconfined quarks into account. They demonstrated that fundamental modes of the resulting hybrid star can be excited and these modes give rise to detectable gravitational wave signals. However, the magnetic field was not considered in these studies. Until recently, we took a magnetic field into account for the first time and investigated the properties of a magnetized hybrid star formed from phase-transition-induced collapse²¹.

In this work, we further extract the gravitational wave signatures from the *phase-transition-induced collapse* of a magnetized neutron star through dynamical simulations, and demonstrate that these signatures can be used to probe the internal magnetic field strength together with the composition of the star for the first time. Specifically, we first find that the waveform is primarily composed of the fundamental $l = 0$ quasi-radial F mode and the fundamental $l = 2$ quadrupolar 2f mode. We then show that the maximum wave amplitude $|h|_{\max}$ increases with the maximum magnetic field strength of the interior toroidal field \mathcal{B}_{\max} until the maximum rest-mass density at bounce $\rho_{\max,b}$ decreases due to the increasing \mathcal{B}_{\max} . We finally demonstrate that measuring the frequency ratio between the two fundamental modes f_{2f}/f_F can infer \mathcal{B}_{\max} and the baryonic mass fraction of matter in the mixed phase M_{mp}/M_0 . Therefore, we use \mathcal{B}_{\max} and M_{mp}/M_0 as two examples to illustrate that analyzing the oscillation modes of neutron stars can provide us information about the interior of the stars.

Results

Waveform

Similar features in the waveform are observed in different simulations (see ‘Simulations’ in the Methods), so we pick one to describe the waveform. Here, we take the simulation with the initial magnetized neutron star model T1K6 (see ‘Initial neutron star models’ in the Methods) and an exponent quantifying the pressure contribution due to deconfined quarks in the mixed phase $\delta = 3$ (see ‘Hybrid star models and evolution’ in the Methods). We plot the time evolution of the gravitational wave amplitude h of a magnetized hybrid star at a distance of 10 kpc (top panel) and the corresponding power spectrum \hat{h} in an arbitrary unit (bottom panel) in Fig. 1. The fundamental $l = 0$ quasi-radial F mode (red dashed line) and the fundamental $l = 2$ quadrupolar 2f mode (green dash-dotted line) are the 2 dominating peaks in the spectrum (see ‘Gravitational wave extraction and mode identification’ in the Methods).

The peak of 2f mode is observed in all models, while the peak of F mode is observed starting from the initial model T1K4. The appearance of the F mode peak is mainly due to the deformation of the star by a strong magnetic field. Similar to the effect of rotation²², the magnetic pressure breaks the spherical symmetry of the star. The radial mode then becomes quasi-radial and can emit gravitational waves.

Wave amplitude

The top panel of Fig. 2 shows the maximum gravitational wave amplitude $|h|_{\max}$ at a distance of 10 kpc against the maximum magnetic field strength of the resulting hybrid star \mathcal{B}_{\max} . The data points are arranged into 3 sequences with 3 values of $\delta \in \{1, 2, 3\}$, where δ is an exponent quantifying the pressure contribution due to quark matter in the mixed phase. First, $|h|_{\max}$ increases with \mathcal{B}_{\max} when $\mathcal{B}_{\max} \lesssim 5 \times 10^{17}$ G. After obtaining a maximum value at $\mathcal{B}_{\max} \sim 5 \times 10^{17}$ G, $|h|_{\max}$ decreases promptly with \mathcal{B}_{\max} . This behavior could be interpreted in respect of magnetic deformation (illustrated as the absolute value of the surface deformation $|\varepsilon_s|$ in the middle panel of Fig. 2) and the oscillation amplitude of the rest-mass density (described by the maximum rest-mass density at bounce $\rho_{\max,b}$ in the bottom panel of Fig. 2). Here, we define the surface deformation as $\varepsilon_s = r_e/r_p - 1$ ⁸, where r_p and r_e are the polar radius and the equatorial radius of the resulting hybrid star respectively. The detailed definitions of the polar and equatorial radius can be found in our previous work of Yip et al.²¹. The maximum rest-mass density at bounce $\rho_{\max,b}$ refers to the peak value of the maximum rest-mass density during the time evolution (Similar to the central rest-mass density at bounce $\rho_{c,b}$ in Abdikamalov et al.¹⁹). According to Eq. (9), the oscillation amplitude of the quadrupole moment depends on both the deformation and the rest-mass density of the star. In the lower \mathcal{B}_{\max} regime, as $|\varepsilon_s|$ increases with \mathcal{B}_{\max} while $\rho_{\max,b}$ is not sensitive to \mathcal{B}_{\max} , which contributes to an increasing quadrupole moment and thus an increasing $|h|_{\max}$. On the other hand, $\rho_{\max,b}$ decreases rapidly when $\mathcal{B}_{\max} \gtrsim 5 \times 10^{17}$ so it greatly reduces the oscillation amplitude of the quadrupole moment and gives a lower $|h|_{\max}$. Furthermore, increasing δ gives a larger $|h|_{\max}$, which could also result from increasing $\rho_{\max,b}$ as δ increases. Accordingly, $|h|_{\max}$ increases with \mathcal{B}_{\max} until $\rho_{\max,b}$ decreases due to the increasing \mathcal{B}_{\max} .

Fundamental mode frequencies

We plot fundamental $l = 0$ quasi-radial mode frequency f_F and fundamental $l = 2$ quadrupolar mode frequency f_{2f} against the maximum magnetic field strength \mathcal{B}_{\max} in Fig. 3. Our data points are arranged into 3 sequences according to values of $\delta \in \{1, 2, 3\}$ used, where δ is an exponent describing the pressure contribution due to quark matter in the mixed phase. The data points of our previous study of Leung et al.²³ are also included as a comparison. The oscillation modes of magnetized neutron stars without deconfined quark matter was considered in Leung et al.. Both fundamental modes decrease similarly to those in Leung et al.. Nonetheless, f_F in our models is smaller while f_{2f} is slightly larger than the models in Leung et al.

when $\mathcal{B}_{\max} \lesssim 5 \times 10^{17}$ G. These frequency differences depend on δ . f_F decreases with δ while f_{2f} increases with it. Hence, the magnetic suppression of stellar oscillations found by Leung et al. is still valid in our magnetized hybrid star models and the mode frequency is also sensitive to δ .

These behaviors of f_F and f_{2f} against δ were also observed in Abdikamalov et al.¹⁹. They investigated the oscillation modes in the gravitational wave signals from the formation of unmagnetized rotating hybrid stars. The decrease in f_F was interpreted as the result of forming a more rapidly rotating hybrid star with a larger δ , leading to a more significant mode suppression by the rotation. With the rediscovery of the fundamental mode behaviors in our models of magnetized non-rotating hybrid stars, these behaviors may be intrinsic properties of such a phase transition or the resulting hybrid star. We plan to investigate this aspect thoroughly in future studies.

Constraining the magnetic field and the composition

To better illustrate the correlation between the fundamental mode frequencies and the properties of the resulting magnetized hybrid star, we plot a contour plot of the frequency ratio between the fundamental $l = 0$ quasi-radial mode and the fundamental $l = 2$ quadrupolar mode f_{2f}/f_F against the maximum magnetic field strength \mathcal{B}_{\max} (horizontal axis) and the baryonic mass fraction of matter in the mixed phase M_{mp}/M_0 (vertical axis) in Fig. 4. We constructed this plot by the cubic radial basis function interpolation of the data points of our models and in our previous work of Leung et al.²³. A colored dot with a black edge labels each data point. The dash-dotted lines denote the contour lines for particular values of f_{2f}/f_F . For a fixed value of f_{2f}/f_F , there are localized regions in the $\mathcal{B}_{\max} - M_{\text{mp}}/M_0$ plane. Therefore, the measurement of f_{2f}/f_F constrains the values of \mathcal{B}_{\max} and M_{mp}/M_0 .

Discussion

In this work, for the first time, we dynamically simulate the collapse of magnetized neutron stars induced by a phase transition and demonstrate that the fundamental modes of neutron stars can be used to constrain the internal magnetic field strength together with the composition of the stars. In particular, we first found that the waveform is primarily composed of the fundamental $l = 0$ quasi-radial F mode and the fundamental $l = 2$ quadrupolar 2f mode. We next investigate the maximum gravitational wave amplitude $|h|_{\max}$. $|h|_{\max}$ firstly rises with \mathcal{B}_{\max} due to the increasing magnetic deformation when $\mathcal{B}_{\max} \lesssim 5 \times 10^{17}$ G. On the other hand, when $\mathcal{B}_{\max} \gtrsim 5 \times 10^{17}$ G, $|h|_{\max}$ decreases substantially with \mathcal{B}_{\max} due to the drop in the oscillation amplitude of the rest-mass density. Then, we have demonstrated that the magnetic suppression of stellar oscillations found in our previous work of Leung et al.²³ remains valid in our models with the mode frequency value being sensitive to the pressure contribution due to quark matter δ . Finally, we have shown that the maximum magnetic field strength \mathcal{B}_{\max} and the baryonic mass fraction of matter in the mixed phase M_{mp}/M_0 could be constrained by measuring the frequency ratio between the 2 fundamental modes f_{2f}/f_F .

The fundamental modes in this work are in the frequency range of $f \sim 600 - 1800$ Hz. Current gravitational wave detectors, including Advanced LIGO²⁴, Advanced Virgo²⁵, and KAGRA^{26,27}, are sensitive to the gravitational wave signals with frequencies of $f \sim 20 - 2000$ Hz. Thus, these detectors can barely detect the higher frequency 2f modes. In contrast, the third-generation gravitational wave detectors, such as the Einstein Telescope (ET)²⁸ and Cosmic Explorer (CE)²⁹⁻³¹, is designed to have a broader sensitivity band with a frequency range of $f \sim 1 - 10000$ Hz. Moreover, it has been shown that the mode frequency of the post-merger signal from binary neutron star coalescences can be measured up to an accuracy of $\sim \mathcal{O}(10)$ Hz with the third-generation gravitational wave detectors³². Hence, we expect the fundamental modes in this work could also be measured in roughly the same order of accuracy using these detectors. However, a detailed analysis targeting the gravitational waves from phase-transition-induced collapses of neutron stars is necessary to verify this claim. This kind of analysis is beyond the scope of this study, so we leave it for future work.

By examining \mathcal{B}_{\max} and M_{mp}/M_0 as an example, this work reveals that studying the fundamental modes of neutron stars can yield important information inside the stars. Several extensions can be made to the current work. Firstly, this can be done using a more realistic equation of state that considers thermal and magnetic effects. Next, other kinds of magnetic field geometries, including purely poloidal fields and twisted torus configurations, should also be investigated. Furthermore, since the instability of the purely toroidal field has been suppressed due to the restriction to axisymmetry in this work, 3D simulations without axisymmetry should also be performed. Finally, it is also necessary to consider the rotation of neutron stars, as different observations suggest that they rotate.

Methods

The set-ups of simulations in this work are identical to those in our previous work of Yip et al.²¹. Here, we briefly highlight these set-ups for completeness.

Initial neutron star models

Equilibrium models of neutron stars in axisymmetry are constructed by the open-sourced code XNS^{33–37}, which are the initial data for the simulations. We construct these equilibrium models with a polytropic equation of state,

$$P = K\rho^\gamma, \quad (1)$$

where P denotes the pressure, ρ denotes the rest-mass density and we adopt a polytropic constant $K = 1.6 \times 10^5 \text{ cm}^5 \text{ g}^{-1} \text{ s}^{-2}$ (which is equivalent to 110 in the unit of $c = G = M_\odot = 1$) and a polytropic index $\gamma = 2$. The specific internal energy ε on the initial time-slice is specified by

$$\varepsilon = \frac{K}{\gamma-1} \rho^{\gamma-1}. \quad (2)$$

The toroidal magnetic field *enclosed in the star* follows a magnetic polytropic law

$$\mathcal{B}_\phi = \alpha^{-1} K_m (\rho h \varpi^2)^m, \quad (3)$$

where α denotes the lapse function, K_m denotes the toroidal magnetization constant, h denotes the specific enthalpy, $\varpi^2 = \alpha^2 \psi^4 r^2 \sin^2 \theta$, ψ denotes the conformal factor, (r, θ) denote the radial and angular coordinates in 2D spherical coordinates, and $m \geq 1$ denotes the toroidal magnetization index.

There are 9 models constructed in total, with ‘REF’ corresponding to the unmagnetized reference model and the others are magnetized neutron star models. These models are included in our previous work of Leung et al.²³. As this work does not aim to study neutron stars with various masses, all models have a fixed baryonic mass of $M_0 = 1.68 M_\odot$, within the mass range of ordinary neutron stars. Also, each magnetized model has the same toroidal magnetization index $m = 1$ but has different values of the toroidal magnetization constant K_m . The models are sorted by increasing maximum magnetic field strength \mathcal{B}_{\max} , where ‘T1K1’ has the lowest field strength, ‘T1K2’ has the second lowest field strength, and so on. (‘T1’ means the toroidal magnetization index $m = 1$ and ‘K’ represents the toroidal magnetization constant K_m .) These models allow for a phase transition within the stellar core and enable comparison with Leung et al.. An overview of the detailed properties of all nine models can be found in Table 1.

Hybrid star models and evolution

Based on the framework introduced by Lin et al.²⁰, we assume that the phase transition happens instantaneously in the initial time slice and is triggered by changing the original polytropic equation to a “softer” equation of state for describing hybrid stars. The MIT bag model equation of state³⁸ for massless and non-interacting quarks is given by

$$P_q = \frac{1}{3}(e - 4B), \quad (4)$$

where P_q denotes the pressure of deconfined quarks, e denotes the total energy density and B denotes the bag constant. We apply the ideal gas equation of state to describe the evolution of normal hadronic matter

$$P_h = (\gamma - 1)\rho\varepsilon, \quad (5)$$

where P_h denotes the pressure of hadrons and γ is chosen to be 2.

A hybrid star formed after the phase-transition-induced collapse can be made up of two or three parts: (i) a hadronic phase for the region having a rest-mass density less than the lower threshold density $\rho < \rho_{\text{hm}}$, (ii) a mixed phase of the deconfined quarks and hadrons for the region having a rest-mass density in between the lower threshold density and the upper threshold density $\rho_{\text{hm}} < \rho < \rho_{\text{qm}}$, and (iii) a region of pure quark matter phase with a rest-mass density beyond $\rho > \rho_{\text{qm}}$ (the maximum density might or might not correspond to this phase in practice).

Following Abdikamalov et al.¹⁹, the equation of state for hybrid stars can be expressed as follows:

$$P = \begin{cases} P_h & \text{for } \rho < \rho_{\text{hm}}, \\ \alpha_q P_q + (1 - \alpha_q) P_h & \text{for } \rho_{\text{hm}} \leq \rho \leq \rho_{\text{qm}}, \\ P_q & \text{for } \rho_{\text{qm}} < \rho, \end{cases} \quad (6)$$

where

$$\alpha_q = 1 - \left(\frac{\rho_{\text{qm}} - \rho}{\rho_{\text{qm}} - \rho_{\text{hm}}} \right)^\delta \quad (7)$$

quantifies the relative contribution of hadrons and deconfined quarks to the total pressure in the mixed phase. By using δ as the exponent, the pressure contribution due to deconfined quarks can be adjusted. We use 3 values of $\delta \in \{1, 2, 3\}$ to vary the pressure contribution due to deconfined quarks in the mixed phase. We take $\rho_{\text{hm}} = 6.97 \times 10^{14} \text{ g cm}^{-3}$, $\rho_{\text{qm}} = 24.3 \times 10^{14} \text{ g cm}^{-3}$ and $B^{1/4} = 170 \text{ MeV}$.

Simulations

Simulations are performed three times for each of the 9 equilibrium models, once for each value of $\delta \in \{1, 2, 3\}$. Thus, $9 \times 3 = 27$ simulations are conducted. The stellar models are evolved in dynamical spacetime using the new general relativistic magnetohydrodynamics code `Gmunu`^{39–41}. `Gmunu` adopts a multigrid method for solving the Einstein equations in the conformally flat condition approximation.

Ideal general-relativistic magnetohydrodynamics simulations are carried out in 2D cylindrical coordinates (R, z) . Axisymmetry with respect to the z -axis and equatorial symmetry are imposed for the simulations. The computational domain covers the region $[0, 100]$ for both R and z directions, with the base grid resolution $N_R \times N_z = 32 \times 32$ and allowing 6 AMR levels (effective resolution = 1024×1024). The refinement criteria of AMR we used are equivalent to those in Cheong et al.⁴⁰ and Leung et al.²³. TVDLF approximate Riemann solver⁴², 3rd-order reconstruction method PPM⁴³ and 3rd-order accurate SSPRK3 time integrator⁴⁴ are used for the simulations. The region surrounding the star is filled with an artificially low-density ‘atmosphere’, with a rest-mass density of $\rho_{\text{atm}} \sim 10^{-10} \rho_c (t = 0)$. In addition, as the simulations are restricted to magnetized stars with a purely toroidal field in axisymmetry, no divergence cleaning method is adopted.

Gravitational wave extraction and mode identification

The gravitational wave signal due to the phase-transition-induced collapse is computed by the quadrupole moment formula for an axisymmetric source⁴⁵

$$h = \frac{1}{2D_{\text{obs}}} (2\ddot{I}_{zz} - \ddot{I}_{RR}), \quad (8)$$

where h is the gravitational wave amplitude observed in the equatorial plane, I_{ij} is the quadrupole moment, \dot{I}_{ij} is its second-time derivative, and D_{obs} is the distance from the source. Since there is no unique choice for the definition of quadrupole moment in dynamical spacetime, we choose⁴⁶

$$I_{ij} = \int \rho_* x^i x^j d^3x, \quad (9)$$

where x^i is the spatial coordinate, $\rho_* \equiv \rho W \sqrt{\gamma}$ is the conserved rest-mass density, ρ is the rest-mass density, $W \equiv 1/\sqrt{1 - v^i v_i}$ is the Lorentz factor, v_i is the 3-velocity and γ_{ij} is the spatial metric. With the continuity equation

$$\partial_t \rho_* + \partial_i (\rho_* \hat{v}^i) = 0, \quad (10)$$

where $\hat{v}^i \equiv (\alpha v^i - \beta^i)$, α is the lapse function and β^i is the space-like shift vector, the first time derivative of quadrupole moment \dot{I}_{ij} can be computed by

$$\dot{I}_{ij} = \int \rho_* (\hat{v}^i x^j + x^i \hat{v}^j) d^3x. \quad (11)$$

The second time derivative \ddot{I}_{ij} is then computed by the finite difference method.

After computing the waveform, we follow the method introduced by Lin et al.²⁰ to identify the fundamental modes in the gravitational wave signal. Specifically, we compare our results with the perturbed equilibrium models in our previous work of Leung et al.²³, which have similar structures to those of the resulting hybrid stars in our simulations.

References

1. Kouveliotou, C. *et al.* An X-ray pulsar with a superstrong magnetic field in the soft γ -ray repeater SGR1806 - 20. *Nature* **393**, 235–237, DOI: [10.1038/30410](https://doi.org/10.1038/30410) (1998).
2. Hurley, K. *et al.* ASCA Discovery of an X-Ray Pulsar in the Error Box of SGR 1900+14. *Astrophys. J. Lett.* **510**, L111–L114, DOI: [10.1086/311820](https://doi.org/10.1086/311820) (1999). [astro-ph/9811388](https://arxiv.org/abs/astro-ph/9811388).
3. Mereghetti, S. & Stella, L. The Very Low Mass X-Ray Binary Pulsars: A New Class of Sources? *Astrophys. J. Lett.* **442**, L17, DOI: [10.1086/187805](https://doi.org/10.1086/187805) (1995).

4. Mereghetti, S., Cremonesi, D., Feroci, M. & Tavani, M. BeppoSAX observations of SGR 1806-20 SAX observations of SGR 1806-20. *Astron. Astrophys.* **361**, 240–244 (2000).
5. van Paradijs, J., Taam, R. E. & van den Heuvel, E. P. J. On the nature of the ‘anomalous’ 6-s X-ray pulsars. *Astron. Astrophys.* **299**, L41 (1995).
6. Kiuchi, K. & Yoshida, S. Relativistic stars with purely toroidal magnetic fields. *Phys. Rev. D* **78**, 044045, DOI: [10.1103/PhysRevD.78.044045](https://doi.org/10.1103/PhysRevD.78.044045)[10.48550/arXiv.0802.2983](https://arxiv.org/abs/0802.2983) (2008). [0802.2983](https://arxiv.org/abs/0802.2983).
7. Kiuchi, K., Kotake, K. & Yoshida, S. Equilibrium Configurations of Relativistic Stars with Purely Toroidal Magnetic Fields: Effects of Realistic Equations of State. *Astrophys. J.* **698**, 541–557, DOI: [10.1088/0004-637X/698/1/541](https://doi.org/10.1088/0004-637X/698/1/541)[10.48550/arXiv.0904.2044](https://arxiv.org/abs/0904.2044) (2009). [0904.2044](https://arxiv.org/abs/0904.2044).
8. Friebe, J. & Rezzolla, L. Equilibrium models of relativistic stars with a toroidal magnetic field. *Mon. Not. R. Astron. Soc.* **427**, 3406–3426, DOI: [10.1111/j.1365-2966.2012.22027.x](https://doi.org/10.1111/j.1365-2966.2012.22027.x)[10.48550/arXiv.1207.4035](https://arxiv.org/abs/1207.4035) (2012). [1207.4035](https://arxiv.org/abs/1207.4035).
9. Bocquet, M., Bonazzola, S., Gourgoulhon, E. & Novak, J. Rotating neutron star models with a magnetic field. *Astron. Astrophys.* **301**, 757, DOI: [10.48550/arXiv.gr-qc/9503044](https://doi.org/10.48550/arXiv.gr-qc/9503044) (1995). [gr-qc/9503044](https://arxiv.org/abs/gr-qc/9503044).
10. Konno, K. Moments of inertia of relativistic magnetized stars. *Astron. Astrophys.* **372**, 594–600, DOI: [10.1051/0004-6361:200105561](https://doi.org/10.1051/0004-6361:200105561)[10.48550/arXiv.gr-qc/0105015](https://arxiv.org/abs/0105015) (2001). [gr-qc/0105015](https://arxiv.org/abs/gr-qc/0105015).
11. Yazadjiev, S. S. Relativistic models of magnetars: Nonperturbative analytical approach. *Phys. Rev. D* **85**, 044030, DOI: [10.1103/PhysRevD.85.044030](https://doi.org/10.1103/PhysRevD.85.044030)[10.48550/arXiv.1111.3536](https://arxiv.org/abs/1111.3536) (2012). [1111.3536](https://arxiv.org/abs/1111.3536).
12. Bonazzola, S. & Gourgoulhon, E. Gravitational waves from pulsars: emission by the magnetic-field-induced distortion. *Astron. Astrophys.* **312**, 675–690, DOI: [10.48550/arXiv.astro-ph/9602107](https://doi.org/10.48550/arXiv.astro-ph/9602107) (1996). [astro-ph/9602107](https://arxiv.org/abs/astro-ph/9602107).
13. Chung, C. T. Y. & Melatos, A. Stokes tomography of radio pulsar magnetospheres - I. Linear polarization. *Mon. Not. R. Astron. Soc.* **411**, 2471–2529, DOI: [10.1111/j.1365-2966.2010.17858.x](https://doi.org/10.1111/j.1365-2966.2010.17858.x) (2011). [1010.2816](https://arxiv.org/abs/1010.2816).
14. Chung, C. T. Y. & Melatos, A. Stokes tomography of radio pulsar magnetospheres - II. Millisecond pulsars. *Mon. Not. R. Astron. Soc.* **415**, 1703–1737, DOI: [10.1111/j.1365-2966.2011.18815.x](https://doi.org/10.1111/j.1365-2966.2011.18815.x) (2011). [1104.1016](https://arxiv.org/abs/1104.1016).
15. Bilous, A. V. *et al.* A NICER View of PSR J0030+0451: Evidence for a Global-scale Multipolar Magnetic Field. *Astrophys. J. Lett.* **887**, L23, DOI: [10.3847/2041-8213/ab53e7](https://doi.org/10.3847/2041-8213/ab53e7) (2019). [1912.05704](https://arxiv.org/abs/1912.05704).
16. de Lima, R. C. R., Coelho, J. G., Pereira, J. P., Rodrigues, C. V. & Rueda, J. A. Evidence for a Multipolar Magnetic Field in SGR J1745-2900 from X-Ray Light-curve Analysis. *Astrophys. J.* **889**, 165, DOI: [10.3847/1538-4357/ab65f4](https://doi.org/10.3847/1538-4357/ab65f4) (2020). [1912.12336](https://arxiv.org/abs/1912.12336).
17. Abbott, B. P. *et al.* GW170817: Observation of Gravitational Waves from a Binary Neutron Star Inspiral. *Phys. Rev. Lett.* **119**, 161101, DOI: [10.1103/PhysRevLett.119.161101](https://doi.org/10.1103/PhysRevLett.119.161101) (2017). [1710.05832](https://arxiv.org/abs/1710.05832).
18. Weber, F. Quark matter in neutron stars. *J. Phys. G Nucl. Phys.* **25**, R195–R229 (1999).
19. Abdikamalov, E. B., Dimmelmeier, H., Rezzolla, L. & Miller, J. C. Relativistic simulations of the phase-transition-induced collapse of neutron stars. *Mon. Not. R. Astron. Soc.* **392**, 52–76, DOI: [10.1111/j.1365-2966.2008.14056.x](https://doi.org/10.1111/j.1365-2966.2008.14056.x) (2009). [0806.1700](https://arxiv.org/abs/0806.1700).
20. Lin, L. M., Cheng, K. S., Chu, M. C. & Suen, W. M. Gravitational Waves from Phase-Transition-Induced Collapse of Neutron Stars. *Astrophys. J.* **639**, 382–396, DOI: [10.1086/499202](https://doi.org/10.1086/499202) (2006). [astro-ph/0509447](https://arxiv.org/abs/astro-ph/0509447).
21. Yip, A. K. L., Chi-Kit Cheong, P. & Li, T. G. F. General-relativistic simulations of the formation of a magnetized hybrid star. *arXiv e-prints* arXiv:2303.16820 (2023). [2303.16820](https://arxiv.org/abs/2303.16820).
22. Chau, W.-Y. Gravitational radiation from neutron stars. *The Astrophys. J.* **147**, 664 (1967).
23. Leung, M. Y., Yip, A. K. L., Cheong, P. C.-K. & Li, T. G. F. Oscillations of highly magnetized non-rotating neutron stars. *Commun. Phys.* **5**, 334, DOI: [10.1038/s42005-022-01112-w](https://doi.org/10.1038/s42005-022-01112-w) (2022).
24. LIGO Scientific Collaboration *et al.* Advanced LIGO. *Class. Quantum Gravity* **32**, 074001, DOI: [10.1088/0264-9381/32/7/074001](https://doi.org/10.1088/0264-9381/32/7/074001) (2015). [1411.4547](https://arxiv.org/abs/1411.4547).
25. Acernese, F. *et al.* Advanced Virgo: a second-generation interferometric gravitational wave detector. *Class. Quantum Gravity* **32**, 024001, DOI: [10.1088/0264-9381/32/2/024001](https://doi.org/10.1088/0264-9381/32/2/024001) (2015). [1408.3978](https://arxiv.org/abs/1408.3978).
26. Somiya, K. Detector configuration of KAGRA-the Japanese cryogenic gravitational-wave detector. *Class. Quantum Gravity* **29**, 124007, DOI: [10.1088/0264-9381/29/12/124007](https://doi.org/10.1088/0264-9381/29/12/124007) (2012). [1111.7185](https://arxiv.org/abs/1111.7185).

27. Aso, Y. *et al.* Interferometer design of the KAGRA gravitational wave detector. *Phys. Rev. D* **88**, 043007, DOI: [10.1103/PhysRevD.88.043007](https://doi.org/10.1103/PhysRevD.88.043007) (2013). [1306.6747](https://arxiv.org/abs/1306.6747).
28. Punturo, M. *et al.* The Einstein Telescope: a third-generation gravitational wave observatory. *Class. Quantum Gravity* **27**, 194002, DOI: [10.1088/0264-9381/27/19/194002](https://doi.org/10.1088/0264-9381/27/19/194002) (2010).
29. Abbott, B. P. *et al.* Exploring the sensitivity of next generation gravitational wave detectors. *Class. Quantum Gravity* **34**, 044001, DOI: [10.1088/1361-6382/aa51f4](https://doi.org/10.1088/1361-6382/aa51f4) (2017). [1607.08697](https://arxiv.org/abs/1607.08697).
30. Reitze, D., LIGO Laboratory: California Institute of Technology, LIGO Laboratory: Massachusetts Institute of Technology, LIGO Hanford Observatory & LIGO Livingston Observatory. The US Program in Ground-Based Gravitational Wave Science: Contribution from the LIGO Laboratory. *Bull. Am. Astron. Soc.* **51**, 141, DOI: [10.48550/arXiv.1903.04615](https://doi.org/10.48550/arXiv.1903.04615) (2019). [1903.04615](https://arxiv.org/abs/1903.04615).
31. Reitze, D. *et al.* Cosmic Explorer: The U.S. Contribution to Gravitational-Wave Astronomy beyond LIGO. In *Bulletin of the American Astronomical Society*, vol. 51, 35, DOI: [10.48550/arXiv.1907.04833](https://doi.org/10.48550/arXiv.1907.04833) (2019). [1907.04833](https://arxiv.org/abs/1907.04833).
32. Yang, H. *et al.* Gravitational wave spectroscopy of binary neutron star merger remnants with mode stacking. *Phys. Rev. D* **97**, 024049, DOI: [10.1103/PhysRevD.97.024049](https://doi.org/10.1103/PhysRevD.97.024049) (2018). [1707.00207](https://arxiv.org/abs/1707.00207).
33. Bucciantini, N. & Del Zanna, L. General relativistic magnetohydrodynamics in axisymmetric dynamical spacetimes: the X-ECHO code. *Astron. Astrophys.* **528**, A101, DOI: [10.1051/0004-6361/201015945](https://doi.org/10.1051/0004-6361/201015945) (2011). [1010.3532](https://arxiv.org/abs/1010.3532).
34. Pili, A. G., Bucciantini, N. & Del Zanna, L. Axisymmetric equilibrium models for magnetized neutron stars in General Relativity under the Conformally Flat Condition. *Mon. Not. R. Astron. Soc.* **439**, 3541–3563, DOI: [10.1093/mnras/stu215](https://doi.org/10.1093/mnras/stu215) (2014). [1401.4308](https://arxiv.org/abs/1401.4308).
35. Pili, A. G., Bucciantini, N. & Del Zanna, L. General relativistic neutron stars with twisted magnetosphere. *Mon. Not. R. Astron. Soc.* **447**, 2821–2835, DOI: [10.1093/mnras/stu2628](https://doi.org/10.1093/mnras/stu2628) (2015). [1412.4036](https://arxiv.org/abs/1412.4036).
36. Pili, A. G., Bucciantini, N. & Del Zanna, L. General relativistic models for rotating magnetized neutron stars in conformally flat space-time. *Mon. Not. R. Astron. Soc.* **470**, 2469–2493, DOI: [10.1093/mnras/stx1176](https://doi.org/10.1093/mnras/stx1176) (2017). [1705.03795](https://arxiv.org/abs/1705.03795).
37. Soldateschi, J., Bucciantini, N. & Del Zanna, L. Axisymmetric equilibrium models for magnetised neutron stars in scalar-tensor theories. *Astron. Astrophys.* **640**, A44, DOI: [10.1051/0004-6361/202037918](https://doi.org/10.1051/0004-6361/202037918) (2020). [2005.12758](https://arxiv.org/abs/2005.12758).
38. Johnson, K. *et al.* The mit bag model. *Acta Phys. Pol. B* **6**, 8 (1975).
39. Cheong, P. C.-K., Lin, L.-M. & Li, T. G. F. Gmunu: toward multigrid based Einstein field equations solver for general-relativistic hydrodynamics simulations. *Class. Quantum Gravity* **37**, 145015, DOI: [10.1088/1361-6382/ab8e9c](https://doi.org/10.1088/1361-6382/ab8e9c) (2020). [2001.05723](https://arxiv.org/abs/2001.05723).
40. Cheong, P. C.-K., Lam, A. T.-L., Ng, H. H.-Y. & Li, T. G. F. Gmunu: paralleled, grid-adaptive, general-relativistic magnetohydrodynamics in curvilinear geometries in dynamical space-times. *Mon. Not. R. Astron. Soc.* **508**, 2279–2301, DOI: [10.1093/mnras/stab2606](https://doi.org/10.1093/mnras/stab2606) (2021). [2012.07322](https://arxiv.org/abs/2012.07322).
41. Cheong, P. C.-K., Pong, D. Y. T., Yip, A. K. L. & Li, T. G. F. An Extension of Gmunu: General-relativistic Resistive Magnetohydrodynamics Based on Staggered-meshed Constrained Transport with Elliptic Cleaning. *Astrophys. J. Suppl. Ser.* **261**, 22, DOI: [10.3847/1538-4365/ac6cec](https://doi.org/10.3847/1538-4365/ac6cec) (2022). [2110.03732](https://arxiv.org/abs/2110.03732).
42. Tóth, G. & Odstrčil, D. Comparison of Some Flux Corrected Transport and Total Variation Diminishing Numerical Schemes for Hydrodynamic and Magnetohydrodynamic Problems. *J. Comput. Phys.* **128**, 82–100, DOI: [10.1006/jcph.1996.0197](https://doi.org/10.1006/jcph.1996.0197) (1996).
43. Colella, P. & Woodward, P. R. The Piecewise Parabolic Method (PPM) for Gas-Dynamical Simulations. *J. Comput. Phys.* **54**, 174–201, DOI: [10.1016/0021-9991\(84\)90143-8](https://doi.org/10.1016/0021-9991(84)90143-8) (1984).
44. Shu, C.-W. & Osher, S. Efficient Implementation of Essentially Non-oscillatory Shock-Capturing Schemes. *J. Comput. Phys.* **77**, 439–471, DOI: [10.1016/0021-9991\(88\)90177-5](https://doi.org/10.1016/0021-9991(88)90177-5) (1988).
45. Shibata, M. *Numerical Relativity* (World Scientific, 2016).
46. Shibata, M. & Sekiguchi, Y.-I. Gravitational waves from axisymmetrically oscillating neutron stars in general relativistic simulations. *Phys. Rev. D* **68**, 104020, DOI: [10.1103/PhysRevD.68.104020](https://doi.org/10.1103/PhysRevD.68.104020) (2003). [astro-ph/0402184](https://arxiv.org/abs/astro-ph/0402184).

Acknowledgements

We acknowledge the support of the CUHK Central High-Performance Computing Cluster, on which the simulations in this work have been performed. This work was partially supported by grants from the Research Grants Council of Hong Kong (Project No. CUHK 14306419), the Croucher Innovation Award from the Croucher Foundation Hong Kong, and the Direct Grant for Research from the Research Committee of The Chinese University of Hong Kong. P.C.K.C. acknowledges support from NSF Grant PHY-2020275 (Network for Neutrinos, Nuclear Astrophysics, and Symmetries (N3AS)).

Author contributions statement

A.K.L.Y. contributed to project planning, simulations, simulation analysis, interpretation of results, and manuscript preparation. P.C.K.C. conceived the idea for the project and contributed to project planning and leadership, simulation code development, interpretation, and manuscript preparation. T.G.F.L. led the group. All authors reviewed the manuscript.

Data availability

The data generated and analysed during this study are available from the corresponding author on reasonable request.

Competing interests statement

The authors declare no competing interests.

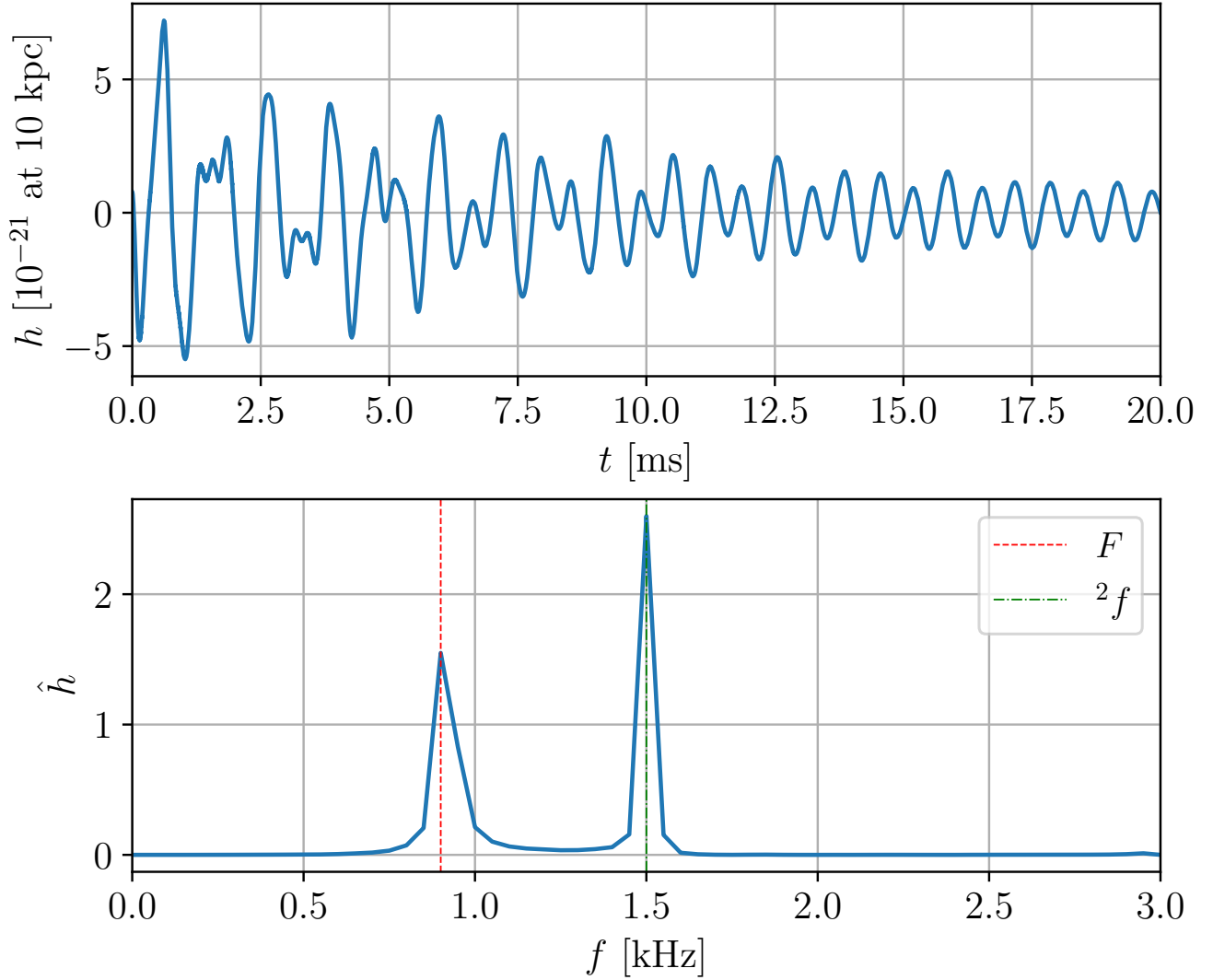


Figure 1. Time evolution of the gravitational wave amplitude h of a magnetized hybrid star at a distance of 10 kpc (top panel) and the corresponding power spectrum \hat{h} in an arbitrary unit (bottom panel) for the simulation with the initial model T1K6 (i.e. Initial maximum magnetic field strength $\mathcal{B}_{\text{max}} = 5.52 \times 10^{17}$ G) and an exponent quantifying the pressure contribution due to quark matter in the mixed phase $\delta = 3$. Two dominating peaks are primarily observed in the spectrum, corresponding to the fundamental $l = 0$ quasi-radial F mode (red dashed line) and the fundamental $l = 2$ quadrupolar 2f mode (green dash-dotted line).

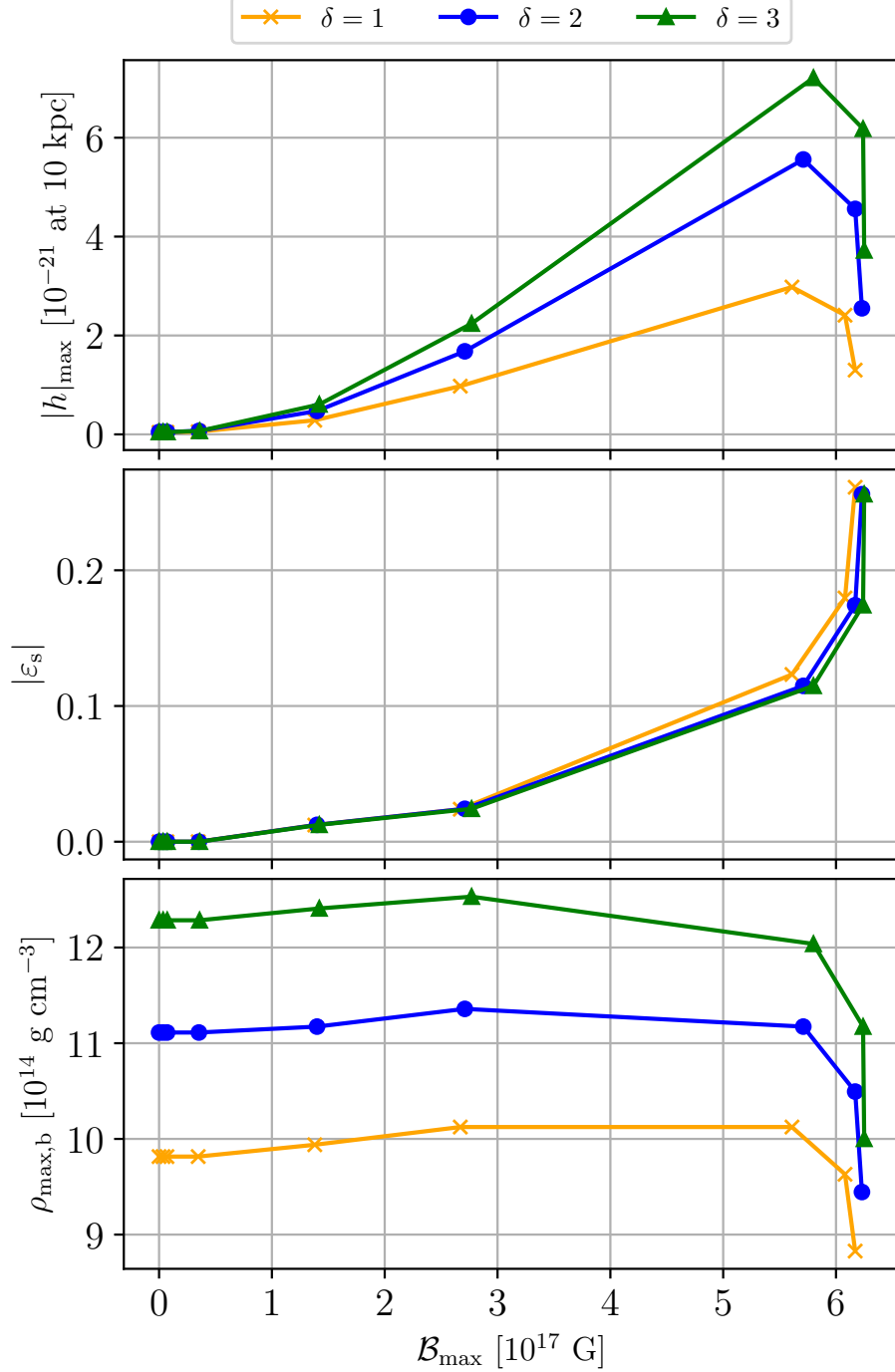


Figure 2. The maximum gravitational wave amplitude $|h|_{\max}$ at a distance of 10 kpc (top panel), the absolute value of the surface deformation $|\varepsilon_s|$ (middle panel), and the maximum rest-mass density at bounce $\rho_{\max,b}$ (bottom panel) against the maximum magnetic field strength \mathcal{B}_{\max} . The data points are arranged into 3 sequences with 3 values of δ in $\{1,2,3\}$, where δ is an exponent describing the pressure contribution due to quark matter in the mixed phase. $|h|_{\max}$ first increases with \mathcal{B}_{\max} when $\mathcal{B}_{\max} \lesssim 5 \times 10^{17}$ G. After reaching a maximum value at $\mathcal{B}_{\max} \sim 5 \times 10^{17}$ G, $|h|_{\max}$ drops rapidly with \mathcal{B}_{\max} . This behavior could be understood in terms of the magnetic deformation (illustrated as $|\varepsilon_s|$ here) and the oscillation amplitude of the rest-mass density (described by $\rho_{\max,b}$). As described by Eq. (9), the oscillation amplitude of the quadrupole moment depends on both the deformation and the rest-mass density of the star. In the lower \mathcal{B}_{\max} regime, as $|\varepsilon_s|$ increases with \mathcal{B}_{\max} while $\rho_{\max,b}$ is not sensitive to \mathcal{B}_{\max} , which contributes to an increasing quadrupole moment and thus an increasing $|h|_{\max}$. On the other hand, $\rho_{\max,b}$ decreases rapidly when $\mathcal{B}_{\max} \gtrsim 5 \times 10^{17}$ so it greatly reduces the oscillation amplitude of the quadrupole moment and gives a lower $|h|_{\max}$. Furthermore, increasing δ gives a larger $|h|_{\max}$, which could also result from increasing $\rho_{\max,b}$ as δ increases. Hence, $|h|_{\max}$ increases with \mathcal{B}_{\max} until $\rho_{\max,b}$ decreases due to the increasing \mathcal{B}_{\max} .

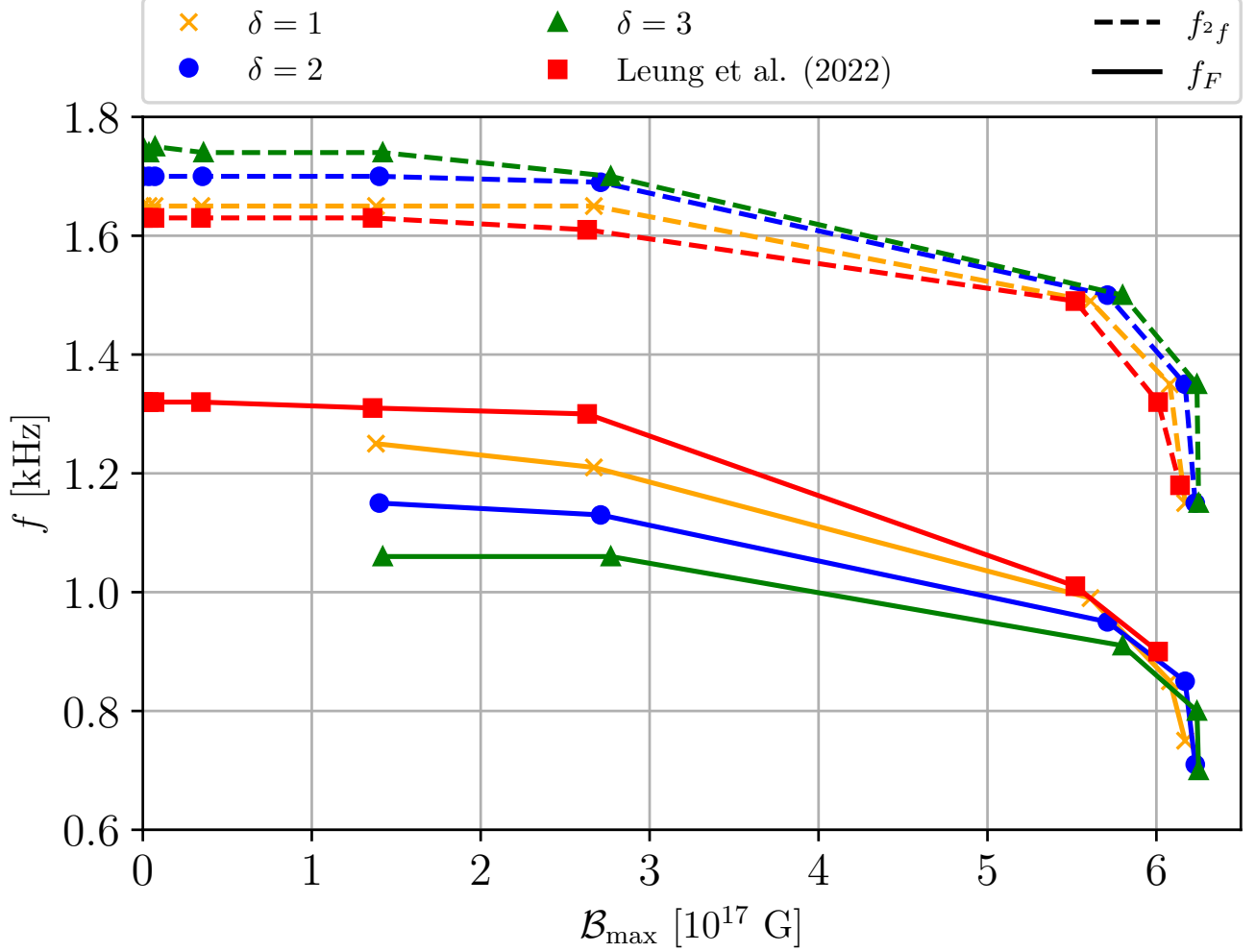


Figure 3. Fundamental $l = 0$ quasi-radial mode frequency f_F and fundamental $l = 2$ quadrupolar mode frequency f_{2f} against the maximum magnetic field strength B_{\max} . Our data points are arranged into 3 sequences according to values of δ in $\{1,2,3\}$ used, where δ is an exponent describing the pressure contribution due to quark matter in the mixed phase. We also include the data points of our previous study of Leung et al.²³ to compare with our results. The fundamental modes of magnetized neutron stars without deconfined quark matter was considered in Leung et al.. A similar decreasing trend for both fundamental modes to those in Leung et al. is observed. However, f_F in our models is smaller while f_{2f} is slightly larger than the models in Leung et al. when $B_{\max} \lesssim 5 \times 10^{17}$ G. These frequency differences are sensitive to δ . f_F decreases with δ while f_{2f} increases with it. Thus, the magnetic suppression of stellar oscillations found by Leung et al. is still valid in our magnetized hybrid star models and the mode frequency is also sensitive to δ .

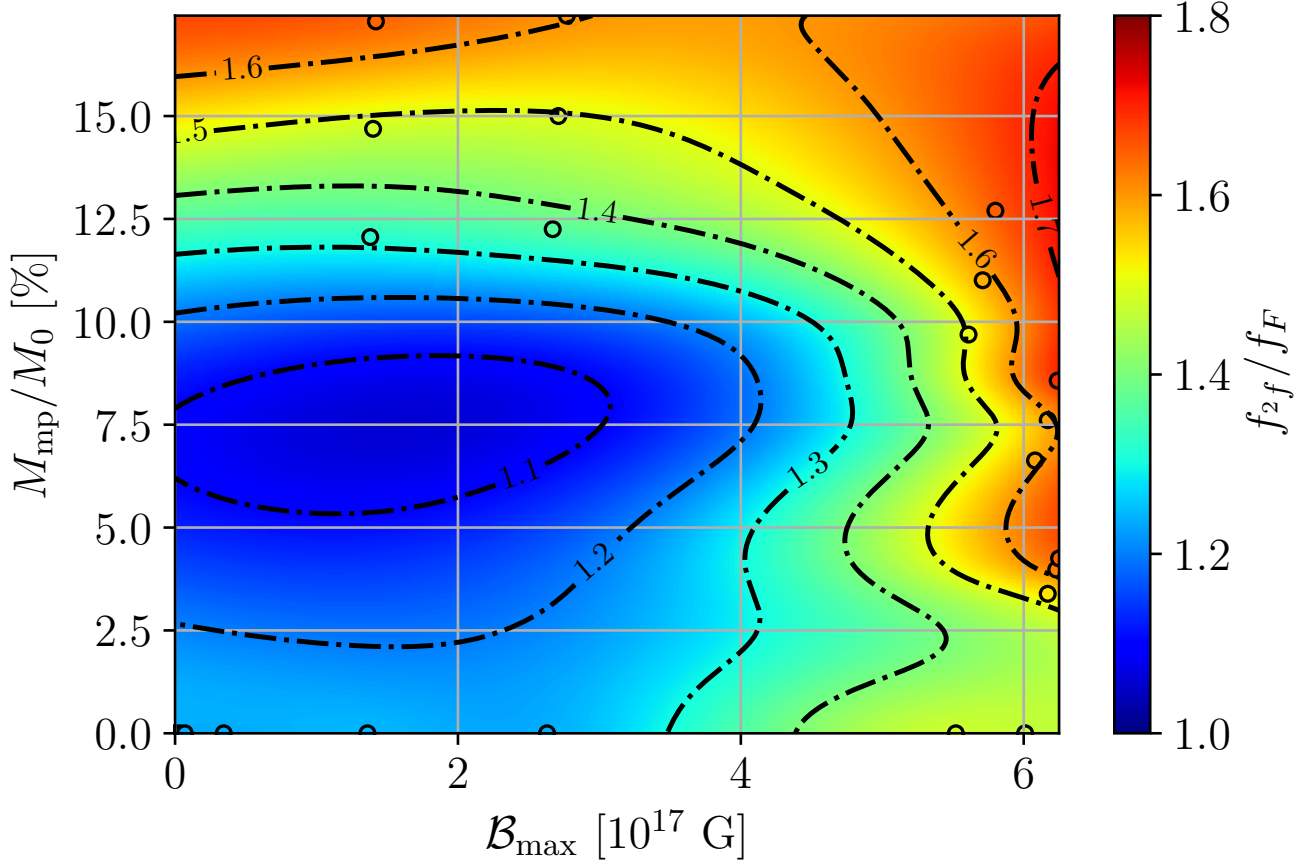


Figure 4. Contour plot of the frequency ratio between the fundamental $l = 0$ quasi-radial mode and the fundamental $l = 2$ quadrupolar mode f_{2f}/f_F against the maximum magnetic field strength \mathcal{B}_{\max} (horizontal axis) and the baryonic mass fraction of matter in the mixed phase M_{mp}/M_0 (vertical axis). This plot is constructed by the cubic radial basis function interpolation of the data points of our models and our previous work of Leung et al.²³. The fundamental modes of magnetized neutron stars without deconfined quark matter was considered in Leung et al.. Each data point is labeled by a colored dot with a black edge. The dash-dotted lines denote the contour lines for particular values of f_{2f}/f_F . Values of f_{2f}/f_F are located in specific regions of the $\mathcal{B}_{\max} - M_{\text{mp}}/M_0$ plane. In consequence, measuring f_{2f}/f_F allows one to infer the value of \mathcal{B}_{\max} and M_{mp}/M_0 .

Model	ρ_c ($10^{14} \text{ g cm}^{-3}$)	M_g (M_\odot)	r_e (km)	\mathcal{B}_{\max} (10^{17} G)
REF	8.56	1.55	11.85	0.00
T1K1	8.56	1.55	11.85	3.45×10^{-2}
T1K2	8.56	1.55	11.85	6.89×10^{-2}
T1K3	8.57	1.55	11.85	3.44×10^{-1}
T1K4	8.63	1.55	11.92	1.36
T1K5	8.81	1.56	12.15	2.63
T1K6	9.10	1.58	14.43	5.52
T1K7	8.81	1.59	16.21	6.01
T1K8	8.27	1.60	18.64	6.14

Table 1. Properties of the 9 initial neutron star models constructed by the XNS code^{33–37}. All numerical values are rounded off to two decimal places. ρ_c is the central rest-mass density, M_g is the gravitational mass, r_e is the equatorial radius, and \mathcal{B}_{\max} is the maximum toroidal field strength inside the neutron star. All the models have a fixed baryonic mass $M_0 = 1.68 M_\odot$ and the 8 magnetized models also have the same toroidal magnetization index $m = 1$.